Hydrodynamic coarsening in phase-separated silicate melts

David Bouttes Bouttes, Océane Lambert, Corinne Claireaux Claireaux, William Woelffel, Davy Dalmas, Emmanuelle Gouillart, Pierre Lhuissier, Luc Salvo, Elodie Boller, Damien Vandembroucq

To cite this version:

David Bouttes Bouttes, Océane Lambert, Corinne Claireaux Claireaux, William Woelffel, Davy Dalmas, et al.. Hydrodynamic coarsening in phase-separated silicate melts. Acta Materialia, 2015, 92, pp.233-242. 10.1016/j.actamat.2015.03.045 . hal-01184915

HAL Id: hal-01184915
https://hal.science/hal-01184915v1

arXiv:1502.03719v1 [cond-mat.mtrl-sci] 12 Feb 2015

Hydrodynamic coarsening in phase-separated silicate melts

David Bouttes

Laboratoire PMMH, UMR 7636 CNRS/ESPCI/Univ. Paris 6 UPMC/Univ. Paris 7 Diderot, 10 rue Vauquelin, 75231 Paris cedex 05, France

Océane Lambert, Corinne Claireaux, William Woelffel, Davy Dalmas, Emmanuelle Gouillart [1]

Surface du Verre et Interfaces, UMR 125 CNRS/Saint-Gobain, 93303 Aubervilliers, France

Pierre Lhuissier, Luc Salvo

SIMAP, GPM2 group, CNRS UMR 5266, University of Grenoble 38402 Saint Martin d'Hères France

Elodie Boller

European Synchrotron Radiation Facility (ESRF), BP 220, 38043 Grenoble, France

Damien Vandembroucq

Laboratoire PMMH, UMR 7636 CNRS/ESPCI/Univ. Paris 6 UPMC/Univ. Paris 7 Diderot, 10 rue Vauquelin, 75231 Paris cedex 05, France

---

Abstract

Using *in-situ* synchrotron tomography, we investigate the coarsening dynamics of barium borosilicate melts during phase separation. The 3-D geometry of the two interconnected phases is determined thanks to image processing. We observe a linear growth of the size of domains with time, at odds with the sublinear diffusive growth usually observed in phase-separating glasses or alloys. Such linear coarsening is attributed to viscous flow inside the bicontinuous phases, and quantitative measurements show that the growth rate is well explained by the ratio of surface tension over viscosity. The geometry of the domains is shown to be statistically similar at different times, provided that the microstructure is rescaled by the average domain size. Complementary experiments on melts with a droplet morphology demonstrate that viscous flow prevails over diffusion in the large range of domain sizes measured in our experiments (1 - 80 μm).

Keywords: phase separation, coarsening, silicate glasses, microtomography

---

1. Introduction

Liquid-liquid phase separation is an appealing mechanism for building materials with tailored microstructure [1]. Molten materials such as polymers [2], silicate melts [3, 4, 5] or metallic alloys [6, 7, 8] exhibit liquid-liquid immiscibility under a critical temperature [9]. During a quench under the immiscibility dome, spinodal decomposition or nucleation and growth are first responsible for the growth of composition fluctuations. Then the size of domains of fixed composition increases in order to minimize interfacial energy – a later stage called *coarsening* [10]. The ability to tune the typical size of the microstructure by controlling coarsening kinetics is paramount for applications of phase separation, among which porous glasses [11] and membranes [12], cellular materials for the food industry [13, 14], core-shell particles [15], quantum dots [16] or super-hydrophobic thin films [17].

For most materials, coarsening results from molecular diffusion through interfaces between the phases, transporting matter from highly-curved interfaces to flatter interfaces. This mechanism oper-

---

[1] corresponding author

ates whatever the topology of the phases – either for interconnected domains or for droplets [18]. Diffusive coarsening is a slow transport mechanism, with the typical domain size growing with time t as $t^{1/3}$. Only limited variations in domain sizes with heating time can therefore be observed in experiments. Amongst inorganic materials, a large body of the phase separation literature is devoted to silicate melts [4]. The seminal theoretical work of Cahn [19] finds its inspiration in the geometry of phase-separated sodium borosilicate glasses. Kinetic studies in silicates evidenced diffusive coarsening both for a droplet [20, 3] and an interconnected microstructure [21]. Because of the limited range of sizes that are observable during a $t^{1/3}$ evolution, a more successful approach for controlling the microstructure size consists in leveraging thermodynamics instead of kinetics, by changing the composition in order to modify the value of the critical temperature. Martel et al. [22], for example, found that the typical size of phase-separated droplets decreased exponentially with alumina content in calcium aluminosilicate glasses. A similar strategy has been applied to metallic glasses [23].

However, another coarsening mechanism has been proposed for larger domain sizes, namely hydrodynamic coarsening, that can occur because of viscous flow driven by Laplace pressure [24]. This regime is characterized by a linear growth of domain sizes with time, that should be much more flexible to tune the microstructure, for a given composition. Several numerical studies [25, 26] have addressed hydrodynamic coarsening; however, experimental observations of this regime are confined to the field of colloid-polymer mixtures [27, 28] and polymers [29, 30], with no single experimental evidence in the field of inorganic materials. Since mechanisms such as crystallization (in alloys and glass-forming melts), gravity or convection and shear often disrupt coarsening and result in different morphologies, one may wonder if a linear growth of domains can be observed at all in inorganic materials.

New insights on phase separation paralleled the emergence of experimental techniques in materials science. Whereas the first kinetic studies were realized in the Fourier space, using light diffusion techniques [31, 1], direct access to the morphology of the phases is now possible thanks to imaging techniques such as electronic microscopy [32], atomic force microscopy [21, 20], X-ray tomography [33] or atom probe tomography [34, 23]. In-situ synchrotron microtomography [35] is a technique of choice for studying microstructure formation [36, 37], since it provides both the 3-D microstructure and its topology, and successive snapshots of its evolution. Recently [38], our team started using in-situ tomography to study phase separation in silicate melts.

In this work, we investigate the coarsening stage of a barium borosilicate glass-forming melt, far above its glass transition. Thanks to in-situ tomography, we evidence a linear growth of the microstructure with time, characteristic of viscous coarsening, that is shown to stem from a series of hydrodynamic pinch-offs. In Section 2, we present the materials and methods used in this work, in particular the characterization of the glasses and the in-situ tomography experiments. Section 3 focuses on the coarsening kinetics during isothermal treatments observed by in-situ microtomography, for an interconnected geometry. Section 4 studies the evolution of the 3-D geometry of the phases during the coarsening process. Finally, we discuss in Section 5 the relative importance of diffusive and viscous transport in our system.

2. Materials and methods

2.1. Glass composition and preparation

In this work, we focus on the ternary diagram $SiO_2 - BaO - B_2O_3$. While alkali borosilicates have been much studied in the literature, alkaline-earth borosilicates are known to have a higher critical temperature, and a larger immiscibility domain [4]. The immiscibility diagram determined by Levin and Cleek [39] is shown in Fig. 1. The critical temperature of the system is above 1470°C, and a large fraction of the immiscibility dome is located above liquidus surfaces (not shown here), resulting in stable liquid-liquid phase separation.

The ternary composition studied here is found in Table 1. It corresponds to a composition well inside the immiscibility domain in order to obtain an interconnected microstructure, and to a liquidus temperature of 1180°C.

In order to study submicronic microstructures, we have studied a second glass composition with a small percentage of alumina [40, 22], denoted as *quaternary glass* in Table 1 and subsequently. Since the quaternary diagram has not yet been characterized in the literature, we determined the dome temperature for this composition by thermal treatments at different temperatures, followed by a rapid quench in water. The dome temperature was estimated to be 1175°C (±25°C).

glass name	SiO_2	BaO	B_2O_3	Al_2O_3
ternary glass	59	21.5	19.5	0
Si-rich phase	80	2.7	17.3	0
1270-Ba-rich phase	43	32	25	0
1070-Ba-rich phase	32.8	41.1	26.1	0
quaternary glass	57	21	20	2
droplet glass	66	14	20	0

Table 1: Composition (in weight percent) of the different barium borosilicate glasses.

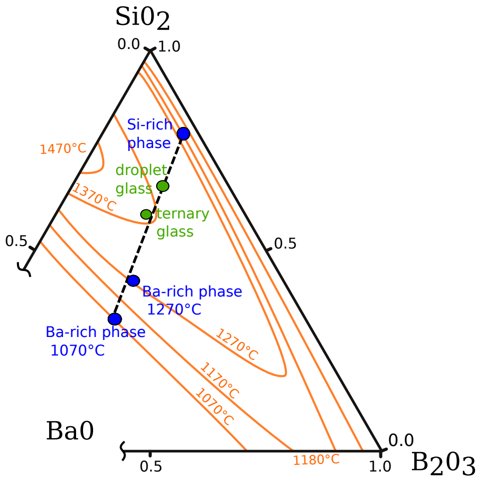

Figure 1: Phase diagram of the $SiO_2-BaO-B_2O_3$ system, in weight fractions. Isotherms of the immiscibility dome (in orange) are plotted after [39], while the tie-line corresponding to composition 1 is drawn from electron microprobe measurements. The composition used in tomography experiments corresponds to the *ternary glass* point.

For the elaboration of the glasses, batches of 1 kg were melted at 1600°C from raw materials (reagent-grade barium carbonate and boric acid, and E400 silica) in a gas-fired lab furnace. Oxygen bubbling was used to ensure a good homogeneity of the melt. Glasses were quenched in air and annealed at 650°C. During the quench from 1600° C to room temperature, a small microstructure appeared because of phase separation. The typical size of this initial microstructure is 5 μm for the ternary glass, and 100 nm for the quaternary glass (because of a much lower dome temperature).

2.2. Tie-line

Determining phase compositions in demixed glasses is usually a difficult endeavour because of the submicronic size of the domains. Typical methods use selective dissolution in acid [41] or compare DSC plots to previously-determined glass-transition isotherms [42], but such methods often lack precision. In our system, large sizes of the domains (several tens of microns) can easily be obtained, which made it possible to analyze the compositions by electron microprobe. Thermal treatments were realized at 1070°C and 1270°C for the ternary glass. The composition of the phases was analyzed using a Cameca SX 100 microprobe at 15 kV and 15 nA. The beam was unfocused with a spot size of 20 μm in order to limit boron migration. The compositions of the phases are given in Table 1 and represented in Fig. 1. Compositions are in agreement with the limits of the immiscibility region proposed by Levin and Cleek [39]. At both temperatures, the glass melt separates in a silica-rich phase and a barium-rich one, the variation of the boron content being much smaller. The precision of the microprobe measurements – of the order of 1 wt% because of the incertitude on boron content – is not sufficient to distinguish between the silica-rich compositions at 1070°C and 1270°C. Interestingly, phases at 1070°C and 1270°C lie on the same tie-line, therefore no tie-line rotation is observed in such a temperature range (contrary to other studies made at lower temperature [43], closer to the glass transition).

2.3. Physical properties

As will be described later, the kinetics of domain coarsening is governed by the ratio between the interfacial tension between the two phases, and the viscosity of the most viscous phase. In order to characterize the physical properties of the separated phases, glasses with the composition of the silica-rich phase, and the barium-rich phases at 1070°C and 1270°C, were melted from raw materials using the same procedure as for the ternary glass.

Viscosity. The viscosities of the barium-rich phases were measured using a high-temperature Couette-

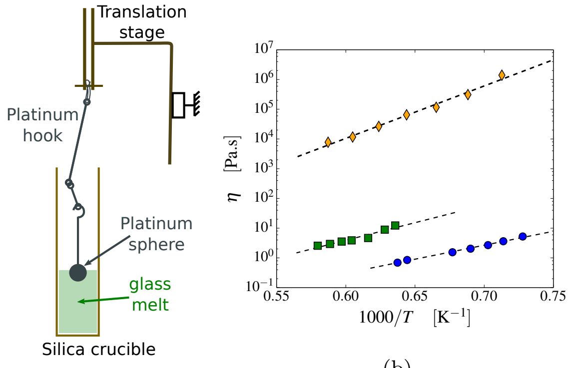

(a) (b)

Figure 2: (a) Schematic of the falling sphere experiment. The diameter of the sphere is 1 cm, and the inner diameter of the crucible is 5 cm. (b) Arrhenian plot of measured viscosities for the silica-rich phase (♦), 1270°-barium-rich phase (■) and 1070°-barium-rich phase (●).

flow apparatus. For the silica-rich phase, the viscosity was too high to use the Couette set-up. We therefore resorted to falling-sphere viscosimetry for the silica-rich phase. Fig. 2 (a) shows a schematic of the experiment. A transparent silica crucible containing the glass melt is placed inside an electric furnace with a transparent silica window. A platinum sphere is tracked with a camera while it falls through the melt, and Stokes' law is used in order to retrieve the viscosity of the melt. Corrections were applied to account for the finite size of the crucible [44] and the accuracy of the method was checked using a soda-lime glass of known viscosity.

The viscosities of the different phases are represented on an Arrhenian plot in Fig. 2 (b). A very important viscosity contrast is observed between the silica-rich phase and the barium-rich phase, up to five orders of magnitude.

In order to supplement viscosity data, dilatometric measurement were realized on the silica-rich phase and the 1070°C-barium-rich phase. The glass transition and the dilatometric softening point (corresponding to a viscosity of about 10^{11}Pa.s) were obtained with this method, with values of respectively 570 and 690°C for the silica-rich phase, and 640 and 670°C for the 1070°-barium-rich phase. Such measures confirm the large extent of the temperature range at which phase separation occurs.

Interfacial tension. We estimated the value of the interfacial tension γ between the two phases to be of the order of 10^{-2} J.m^{-2}, from the comparison of experimental images of the phases and numerical hydrodynamic simulations. The numerical method is described in the Appendix. The order of magnitude is consistent with the scarce literature on measurements of interfacial tension between glassy melts [45, 46], albeit at the lower end of reported values.

Densities. The density of the separated phases were measured from the bulk synthesized glasses, using Archimedes principle. With a density difference of $\Delta\rho \simeq 10^3$ kg.m^{-3} between the Si-rich and the 1070-Ba-rich phase, we estimate the Bond number

$$Bo = \frac{\Delta\rho g l^2}{\gamma} \simeq 10^{-2} \qquad (1)$$

for a typical size ℓ of 100 μm, which is the maximum size that is reached in our coarsening experiments. The Bond number measures the ratio between gravitational and interfacial forces. Its small value means that gravity can be neglected in comparison to Laplace pressure.

2.4. Imaging methods and thermal treatments

In-situ X-ray microtomography experiments were realized at the ID19 beamline of the ESRF synchrotron. The imaged samples were 2-mm-diameter cylinders machined from the bulk ternary glass and put inside 3-mm-outer-diameter alumina crucibles. On the beamline, we used the dedicated "Ecole des Mines" furnace, that can heat millimetric-sized samples to temperatures up to 1500°C. During in-situ experiments, X-rays can get through the furnace thanks to a thin silica window. Samples are glued on top of an alumina rod fixed on a Leuven fast rotation stage, and are allowed to rotate freely inside the fixed furnace thanks to a hole at the bottom of the furnace. At the beginning of a thermal treatment, the sample is introduced into the already hot furnace, ensuring a fast heating rate: we measured that it only takes a few tens of seconds for the sample to reach working temperatures above 1000°C. Isothermal experiments were realized at temperatures ranging from 1030°C to 1330°C.

Pink beam with an energy of 32 keV is used to achieve sufficient transmission. At this energy, the absorption coefficients of the two phases (resp. 0.08 mm^{-1} and 1 mm^{-1} for the silica-rich and the 1070°-barium-rich phases) are very different, resulting in a good absorption contrast that facilitates further image processing. The X-ray photons transmitted through the sample were converted to visible light by a 25 μm-thick LuAG scintillator. The pixel size is 1.1 μm. The PCO Dimax camera is equipped with a fast CMOS detector; acquisition times for one radiography varied from 6 to 30 ms depending on the working temperature, resulting in total acquisition times from 4 to 10 s for the total number of radiographies acquired over a rotation of 180°.

3-D absorption images were reconstructed from the set of radiographies using a standard filtered back-projection algorithm [47]. Python's `scikit-image` [48] was used for further processing of 3-D images. Voxels were attributed to the two phases of the glass using the following segmentation procedure: a first denoising step is realized with a total-variation filter [49]; then the Random Walker algorithm [50] is used to segment the two phases. 3-D visualizations of the minority-phase surface are realized with the Mayavi [51] Python package.

For complementary experiments at scales out of the reach of parallel-beam synchrotron tomography, thermal treatments were realized on centimetric-sized samples in an electric furnace. The samples were quenched and impregnated in an epoxy resin. Cross-sections were polished and imaged with a Zeiss DSM 982 Gemini scanning electron microscope, operated at 20 kV.

3. Viscous coarsening

The typical evolution of a sample is shown on Fig. 3, for a temperature of 1230°C. The surface of the barium-rich phase is represented on Fig. 3, with colors encoding the value of the local mean curvature (from dark green to bright yellow for increasing curvature). The same cubic sub-volume of linear size 250 μm is represented at different times during an in-situ experiment, from 80 to 480 s. In this experiment, the volume fraction of the barium-rich phase is measured to be $49 \pm 1\%$, so that it is in slight minority.

An interconnected microstructure is observed for both phases. The minority barium-rich phase is composed of smooth threads of fluid connected together by thicker nodes. Such an interconnected microstructure is often attributed to spinodal decomposition, however our observations only start when the compositions of the phases are fixed. A few disconnected barium-rich domains are observed as well (and represented in purple in Fig. 3), but they represent a very small volume fraction of the phase (always less than 1 % throughout the experiment). No disconnected domains are ever observed for the silica-rich phase. As time increases, we observe the coarsening of the typical size of the microstructure (Fig. 3), while the morphology of the phases continues to look quite similar to the initial state, up to a rescaling of the typical size.

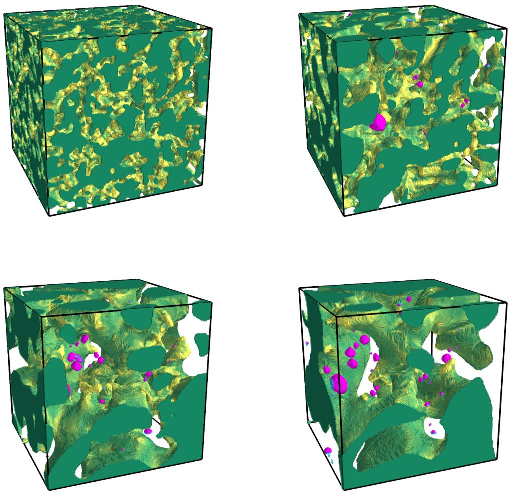

Figure 3: Tomography images of domain coarsening, for an experiment at 1230°C and heating times of 80, 160, 320 and 480 s. The size of the square box is 250 μm. Only the minority (barium-rich) phase is represented. Shades of green encode the local mean curvature, from dark green to yellow. Isolated domains are identified in purple.

We measure the typical size ℓ of the barium-rich phase as its volume $\mathcal{V}$ to surface $\mathcal{S}$ ratio:

$$\ell = \frac{3\mathcal{V}}{\mathcal{S}}, \tag{2}$$

so that ℓ is equal to the radius for a sphere. The surface area is measured from the binarized image thanks to local histograms of voxel configurations, as proposed by Lang et al. [52]. The segmentation process often results in surfaces with a small-scale roughness, at a scale below the true spatial resolution of the experiment. Therefore, the surface is smoothened with a Gaussian filter of standard deviation of 1 pixel before the surface area is computed. This smoothing step reduces the sensitivity of ℓ to the measure and segmentation noise. We have compared ℓ to other measurements of the average local scale derived from the correlation function of the binarized image, or the chord length distribution [53, 54, 1]. All quantities resulted in similar

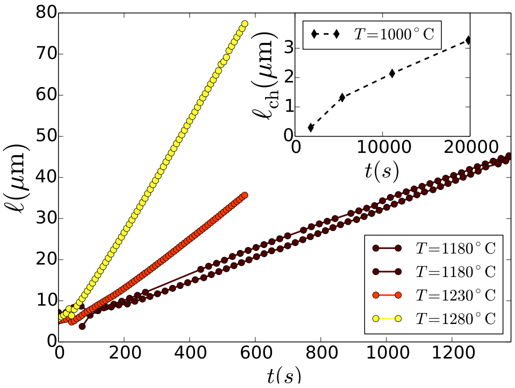

Figure 4: Evolution of the characteristic length $\ell(t)$. Main axes: growth of ℓ measured in in-situ tomography experiments at several temperatures. Inset: growth of ℓ_{ch} measured post-mortem thanks to SEM imaging.

results [55] (up to constant prefactors of order one, coming from the different definitions).

The evolution of ℓ with time is shown on Fig. 4 for experiments realized at different temperatures, from 1180°C to 1280°C. A linear evolution with time is observed, up to typical sizes as high as 80 μm. Since the initial microstructure has a size of about 5 μm, the typical size is multiplied by more than one order of magnitude during the duration of an experiment. The coarsening rate increases with temperature, and several experiments performed at the same temperature show that the value of the coarsening rate is well reproduced (see Fig. 4). In order to characterize the temperature-dependence of the coarsening rate, we have plotted $\dot{\ell}$ in an Arrhenian diagram in Fig. 5, for 11 different experiments realized from 1030 to 1330°C. We observe an Arrhenian temperature dependence, with an activation energy of the order of $300\,\mathrm{kJ.mol}^{-1}$. Since the immiscibility dome widens towards lower temperatures, experiments at different temperatures in Fig. 5 correspond to different volume fractions of the barium-rich phase, from 39 to 52 %. Such variability does not seem to affect the Arrhenian behavior.

In order to test the validity of the linear coarsening regime at smaller scales, we measured the typical size of interconnected phases for thermal treatments at 1000°C of the quaternary glass with alumina, using post-mortem SEM imaging. Since ℓ cannot be directly measured from 2D images, we measured as a proxy for ℓ the average chord size ℓ_{ch}, the chord size distribution [53] being a stereological measure that should be identical in 2D and 3D for statistically isotropic systems. As shown in the inset of Fig. 4, a linear growth of ℓ_{ch} with time is observed for this set of experiments as well, for values of ℓ_{ch} ranging from 1 to 3 μm. The first data point, corresponding to a scale of 300 nm, does not match as well the linear fit. This slight discrepancy at short times and small scales is likely to come from variations in the initial size of the microstructure, since our post-mortem observations were realized on different samples. We conclude that a linear coarsening can be observed at scales ranging from 1 to 80 μm, including scales below the resolution of our tomography experiments.

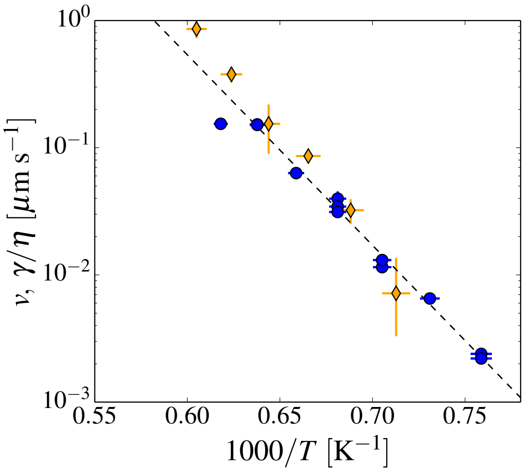

Figure 5: Compararison between experimental and theoretical coarsening rate, plotted in an Arrhenian diagram. Circles: linear growth rates $v = \dot{\ell}$ measured in experiments at temperatures from 1030 to 1330°C. Diamonds: ratio γ/η, determined using the value of γ obtained numerically (see Appendix) and measured viscosities.

The observed linear evolution of ℓ suggests that viscous coarsening dominates over diffusive mechanisms. This may come as a surprise, since diffusive coarsening has been the only mechanism reported so far in silicate melts [4]. 3-D visualizations of the evolution of interfaces (Fig. 6) unravel the local mechanisms resulting in coarsening. Inside curved liquid bridges, Laplace pressure causes fluid to flow from regions with a high mean curvature towards regions with smaller curvatures. This results in a thinning of some liquid bridges (Fig. 6 (b)), up to the break-up of the liquid filament (Fig. 6 (c)). After the break-up, fluid in the broken ends retracts because of capillarity and therefore flows in adja-

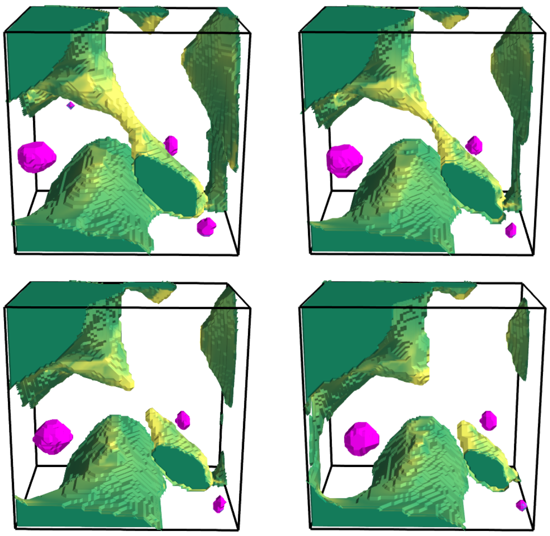

Figure 6: Close-up visualization of a breaking liquid bridge. Surfaces of the percolating domain are color-coded according to mean curvature, from green to yellow. A few disconnected droplets are observed as well (in purple). 3-D images of linear size 140 microns, taken at times 408, 432, 440, and 464 s during an experiment at 1280°C.

cent regions (Fig. 6 (c) and (d)), resulting in a local coarsening. Local break-up events of viscous liquid bridges are also known as *pinch-off* in the fluid mechanics literature [56]. They were observed using confocal microscopy in a colloid-polymer mixture by Aarts and collaborators [27]. Further evidence for the weak influence of diffusion on coarsening is given by the fact that a few isolated domains (displayed in purple in Fig. 3) keep a constant volume through time, so that evaporation can be considered negligible up to the measurement precision. Visual observation also sheds light on the origin of the few isolated domains, that break up from the continuous phase during the retraction of long terminal filaments [38] (see also Fig. 9).

Thanks to such direct observations of coarsening mechanisms, it is possible to revisit the theoretical argument of Siggia [24] for deriving a linear coarsening rate with time. One balances the dominant terms of the Navier-Stokes equation, that are the Laplace pressure gradient and the viscous dissipation, when inertia is negligible:

$$\eta \frac{v}{\ell(t)^2} \sim \frac{p_{\mathrm{Laplace}}}{\ell} \sim \frac{\gamma}{\ell(t)^2}, \tag{3}$$

with η the largest viscosity of the two phases, γ the interfacial tension, v a typical velocity of the fluid and the Laplace pressure $p_{\mathrm{Laplace}} \sim \gamma/l$. Siggia argues that $v \sim \mathrm{d}\ell/\mathrm{d}t$, since ℓ is the typical scale of fluid domains. In Fig. 6, v would be a typical velocity at which fluid flows from the bridge to the node, either when the bridge is still connected or when the broken ends retract. The growth of ℓ in neighboring liquid bridges is due to the redistribution of the fluid from the thinning, then breaking, liquid bridge. Replacing v, one obtains the equation proposed by Siggia:

$$\ell(t) \sim \frac{\gamma}{\eta} t. \tag{4}$$

In order to test whether Eq. (4) describes well the coarsening dynamics observed here, we have compared in Fig. 4 the evolution of the linear prefactor with the evolution with temperature of the ratio γ/η. In Fig. 5, the linear prefactors are plotted in an Arrhenian diagram, for temperatures ranging from 1030 to 1330°C. As for the viscosity, the kinetics of fluid rearrangement can be considered to be governed by the largest viscosity. The estimated interfacial tension over the measured viscosity of the silica-rich phase is therefore superimposed on Fig. 5. We observe a very good agreement between $\dot{\ell}(t)$ and γ/η: the activation energies of the two quantities are very close. Moreover, the proportionality coefficient between $\dot{\ell}(t)$ and γ/η seems to be close to one. The good quantitative agreement between our measurements and Eq. (4) is a convincing evidence that viscous coarsening is a mechanism present in phase-separated silicate melts.

4. Self-similarity of the microstructure

An important hypothesis underlying theoretical descriptions of coarsening is that the geometry of the phases remains statistically the same up to a rescaling of the typical size ℓ – a hypothesis called *dynamic scaling* [57]. In particular, this argument is used by Siggia [24] to justify that $\dot{\ell}$ is equal to the velocity induced by the Laplace pressure.

Statistical characterizations of the domain geometry allow us to test the dynamic scaling hypothesis. In order to characterize the geometry of the system, we compute histograms of surface curvatures, for an experiment at 1180°C. Distributions of curvatures are a common tool for a local characterization of interfaces, in particular for coarsening studies [58, 59]. Principal curvatures κ_1 and κ_2 are computed by fitting a quadric surface to the

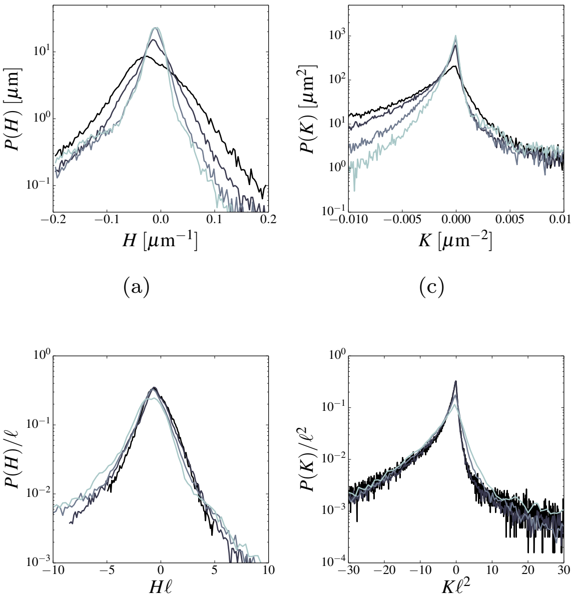

(a) (c)

(b) (d)

Figure 7: Histograms of mean and Gaussian curvatures, for an experiment at 1180°C, observed at thermal treatment times of 15, 28, 48 and 60 min, from dark blue to light blue. (a) Mean curvature H. (b) Renormalized mean curvature $H\ell$. (c) Gaussian curvature K. (d) Renormalized Gaussian curvature $K\ell^2$.

neighbourhood of points lying on the interfacial surface [60, 61]. Mean and Gaussian curvatures are defined respectively by

$$H = \frac{\kappa_1 + \kappa_2}{2}; \quad K = \kappa_1 \kappa_2. \tag{5}$$

Histograms of H and K measured at times from 15 to 60 minutes are plotted in Fig. 7. Histograms of curvatures get narrower with time because of global coarsening, as the characteristic length ℓ grows from 25 to 75 microns from the first to the last image used to build the histograms. The range of curvature values reflects the different possible morphologies of the interfacial surface, with rounded tips ($K > 0$, $H < 0$), tubes ($|K| \ll \ell^{-2}$, $H < 0$) or saddles ($K < 0$). For both H and K, the peak of histograms correspond to tubular morphologies, and the tails to either tips of such tubes, or junctions between them. Fig. 7 (b) and (d) shows the histograms of mean and Gaussian curvatures renormalized by the characteristic length ℓ, $H\ell$ and $K\ell^2$. A good collapse on a master curve is observed both for mean and Gaussian curvature, demonstrating that, statistically speaking, the morphology of the phases does not change over time, except for their average size. The validity of dynamic scaling means that it is possible to elaborate morphologies that are statistically similar, but with sizes that are different. Such property can be interesting for applications but also for designing model materials.

Nevertheless, one should mention that deviations from dynamic scaling can be observed at longer times, because of the progressive fragmentation of disconnected droplets from the percolating low-viscosity phase. Such domains can be observed in Fig. 3 and 6. We have studied deviations from dynamic scaling in a previous paper [38]. Recent work [62] has shown that the fragmentation rate increases drastically when the volume fraction of the low-density phase decreases. In the set of experiments presented here, the volume fraction is large enough that a small fragmentation rate hardly disrupts dynamic scaling for the duration of experiments.

5. Discussion

Our tomography experiments demonstrate that viscous flow induced by Laplace pressure is the prevailing coarsening mechanism over a wide range of lengthscales. Then, why did not previous studies on phase separation in glass-forming melts [63, 21] observe a linear-with-time coarsening? In order to investigate the relative effects of diffusion-induced and viscous-flow-induced coarsening, we carried on a complementary set of experiments where diffusion was the sole coarsening mechanism. To do so, we synthesized a composition on the same tie-line as the ternary glass, but sufficiently off-centered towards the silica-rich phase so that the composition lies inside the binodal domain (see Fig. 1), and is characterized by a droplet morphology (see Fig. 8 (a)). After the quench from the stable region to below the glass transition, a microstructure of barium-rich droplets inside a silica-rich matrix is visible. In the absence of an interconnected minority phase, the prevailing transport mechanism is chemical diffusion through the boundary of the domains (droplets coalescence because of Brownian motion [64] is bound to be slower because of the micronic size of droplets and the very large viscosity of the matrix). Thermal treatments were realized for cm-sized glass cylinders at 1250°C for times ranging from 20 minutes to 6 hours. Polished surfaces cut through the samples were observed post-mortem using SEM imaging. Typical SEM images are shown in Fig. 8 (a). The histogram of areas of the barium-rich droplets was converted to an histogram of volumes of 3-D spheres, using a classical stereologic computation [65]. The evolution of the average domain size with time is shown in Fig. 8 (b); it is consistent with a $t^{1/3}$ evolution. In addition to the different kinetic law, we note that the typical size of droplets is much smaller than for the interconnected structure at a similar temperature (see Fig. 4). This size discrepancy confirms that, when topology allows it, viscous flow is a much more efficient mechanism than diffusion for our system.

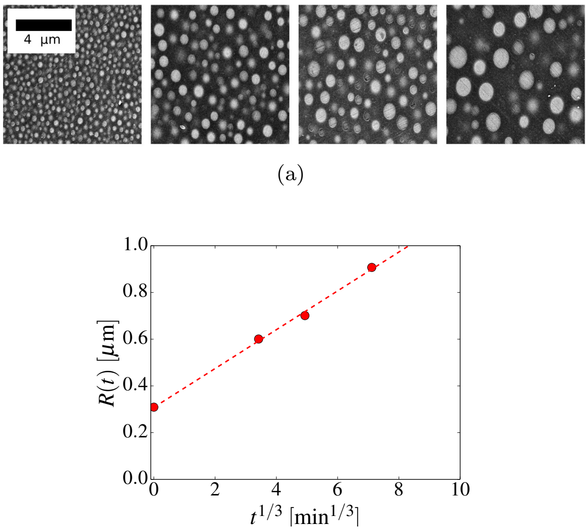

(a)

(b)

Figure 8: (a) SEM images of coarsening for a droplet morphology, for thermal treatments of 0, 20, 120 and 360 min at 1250°C (left to right). (b) Evolution of the average droplet radius with $t^{1/3}$.

For a diffusion-controlled coarsening, diffusion models predict that the growth of ℓ evolves as [10]

$$\ell(t) \sim \left(\frac{\gamma D\Omega}{kT}t\right)^{\frac{1}{3}}, \tag{6}$$

where D is the effective molecular diffusivity, Ω a molecular volume, k the Boltzmann constant and T the temperature. Fitting the size values of Fig. 8 (b) with Eq. (6), we obtain an estimate for the product $D\Omega$. Choosing the molecular volume $\Omega \simeq 10^{-29}\mathrm{m}^3$ gives $D \simeq 2.10^{-12}\,\mathrm{m}^2\mathrm{s}^{-1}$. The theoretical crossover length ℓ^* between diffusive growth and hydrodynamic growth is commonly estimated by equating the interfacial velocity in the two regimes [66], resulting in

$$\ell^* = \sqrt{\frac{\eta D\Omega}{kT}}. \tag{7}$$

For our system at 1250°C, the corresponding numerical values is $\ell^* \simeq 10\,\mathrm{nm}$, much below the initial microstructure size in tomography experiments. The corresponding crossover time $t^* = \frac{kT}{\gamma D\Omega} l^*$ would be of the order of 0.1 s. Observing only the hydrodynamic regime at micronic scales was therefore to be expected.

In this respect, it is instructive to compare such orders of magnitude to the ones of another study [63] where both diffusivity and viscosity were estimated. Simmons et al. [63] measured the evolution of the macroscopic viscosity resulting from coarsening in sodium borosilicate glasses. Using the values obtained for η and D in [63] and Eq. (7), one obtains a crossover scale of a few microns and an hypothetical crossover time of thousands of days. Observing the hydrodynamic regime requires t^* to be accessible in an experiment, and hence the viscosity of the glass not to be too large. Since most previous studies in glass-forming melts were realized slightly above the glass transition, the viscosity was always very high ($> 10^{10}$ Pa.s) and the hydrodynamic regime was out of reach. An interesting perspective of our study would be the investigation of the crossover of the diffusive and hydrodynamic regimes. Such investigations would require to control the critical temperature so that the viscosity just below T_c would result in a crossover time well resolved experimentally.

Let us finally note that simple models relating the viscosity and the diffusivity, such as the Stokes-Einstein relation, or the Eyring model [67] for silicate glasses, result in a crossover length l^* of the same order as a typical molecular size. Observations of diffusive coarsening over larger scales [21, 63] therefore hint at more complex diffusive mechanisms that are decoupled from viscosity – a decoupling that is well known for silicate glasses close to their glass transition [68, 69] and that has been recently discussed for metallic glasses as well [70].

6. Conclusions

Using in-situ microtomography, we have shown that viscous flow prevails as the dominant coarsening mechanism in phase-separated silicate melts, for temperatures far above the glass transition. A linear growth of the typical size has been observed for a large range of scales, from 1 to 80 μm. We have verified that the morphology remains statistically self-similar during coarsening, up to a rescaling by the characteristic size. Whether these mechanisms apply to other inorganic materials, such as phase-separated bulk metallic glasses [7, 71], is an open question of interest for the fundamental understanding of such materials.

The transition between the diffusive and viscous regime is an interesting question open by this work, that will require to understand which diffusive mechanisms control the coarsening at small scales. Future work will focus on smaller volume fractions on the less-viscous phase, for which more fragmentation of droplets is observed.

Acknowledgements

The authors are much grateful to Sophie Schuller for lending them the falling-sphere apparatus for the viscosity measurements. The authors also acknowledge precious help from Yohann Bale, Erick Lamotte, Rudy Vetro and Jean-Paul Valade. This work was supported by the French ANR program “EDDAM” (ANR-11-BS09-027). Experiments were performed on beamline ID19 at ESRF in the framework of projects HD501, SC3724, MA1839 and MA1876.

Appendix: estimation of interfacial tension

In order to estimate the interfacial tension between the two phases, we performed numerical simulations with the Gerris software [72, 73], a finite-volume solver of Navier-Stokes equations. As an initial condition, a mesh was built from the segmentation of a single domain in an experiment at 1180°C (see Fig. 9). Physical parameters of the simulation were set to one, including the size of the box, the interfacial tension between the phases and the viscosity of the most viscous phase. The viscosity of the least viscous phase was set to 10^{-2}, ensuring a high viscosity ratio between the phases. The viscosity ratio in the simulation is not as large as the experimental one, since too large a discrepancy between the two viscosities leads to prohibitive computational times. Such parameters ensure that the Reynolds number is smaller than 0.1. For Reynolds numbers much smaller than 1, in the Stokes flow regime, inertia is negligible and time is only a parameter, with boundary conditions determining completely the further evolution of the system.

Fig. 9 shows the evolution of the initial condition in the experiment, as well as in the simulation of Navier-Stokes equations. A striking similarity is observed between the experimental and numerical geometries. In particular, the domain breaks up at the same place, while the lower end of the domain retracts in both cases. Such observations confirm that hydrodynamic flow is the mechanism responsible for the observed coarsening. Moreover, the proportionality factor needed to adjust experimental and non-dimensional numerical times gives the value of the interfacial tension in the experiment, that is found to be $\gamma = 10^{-2}$J.m^{-2}. We suppose that the interfacial tension does not vary much with temperature, which is a reasonable assumption compared to the much greater variations of the viscosities with temperature.

References

References

[1] P. Levitz, G. Ehret, S. K. Sinha, J. M. Drake, Porous vycor glass: The microstructure as probed by electron

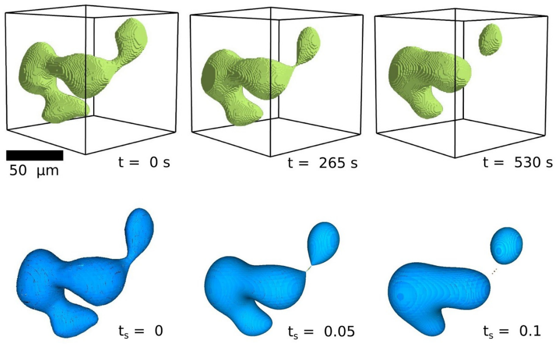

Figure 9: Upper row: evolution of a single domain in an experiment at 1180°C. The size of the square box is 190 μm. Lower row: evolution of the same domain with the Gerris code, with a linear factor between numerical and experimental times chosen to optimize the match between geometries.

microscopy, direct energy transfer, small-angle scattering, and molecular adsorption, Journal of Chemical Physics 95 (8) (1991) 6151.

[2] D. R. Lloyd, S. S. Kim, K. E. Kinzer, Microporous membrane formation via thermally-induced phase separation. II. Liquid-liquid phase separation, Journal of Membrane Science 64 (1) (1991) 1–11.

[3] A. Craievich, E. D. Zanotto, P. F. James, Kinetics of Sub-Liquidus Phase Separation in Silicate and Borate Glasses. A Review, Bull. Soc. Franc. Min. et Crist 106 (1983) 169–84.

[4] O. V. Mazurin, E. A. Porai-Koshits, Phase Separation in Glass, North-Holland, Amsterdam, 1984.

[5] C. Huang, A. Cormack, Structural differences and phase separation in alkali silicate glasses, The Journal of chemical physics 95 (5) (1991) 3634–3642.

[6] E. Davidoff, P. Galenko, D. Herlach, M. Kolbe, N. Wanderka, Spinodally decomposed patterns in rapidly quenched Co–Cu melts, Acta Materialia 61 (4) (2013) 1078–1092.

[7] J. He, N. Mattern, J. Tan, J. Zhao, I. Kaban, Z. Wang, L. Ratke, D. Kim, W. Kim, J. Eckert, A bridge from monotectic alloys to liquid-phase-separated bulk metallic glasses: design, microstructure and phase evolution, Acta Materialia 61 (6) (2013) 2102–2112.

[8] D. Kim, W. Kim, E. Park, N. Mattern, J. Eckert, Phase separation in metallic glasses, Progress in Materials Science 58 (8) (2013) 1103–1172.

[9] R. Balluffi, S. Allen, W. Carter, Kinetics of Materials, John Wiley & Sons, 2005.

[10] A. J. Bray, Theory of phase-ordering kinetics, Advances in Physics 43 (3) (1994) 357–459.

[11] P. Wiltzius, F. S. Bates, S. B. Dierker, G. D. Wignall, Structure of porous Vycor glass, Physical Review A 36 (6) (1987) 2991–2994.

[12] M. Kukizaki, Large-scale production of alkali-resistant Shirasu porous glass (SPG) membranes: Influence of ZrO2 addition on crystallization and phase separation in Na2O-CaO-Al2O3-B2O3-SiO2 glasses; and alkali durability and pore morphology of the membranes, Journal of Membrane Science 360 (1-2) (2010) 426–435.

[13] H. Tanaka, Formation of network and cellular structures by viscoelastic phase separation, Advanced Materials 21 (18) (2009) 1872–1880.

[14] H. Tanaka, Viscoelastic phase separation in soft matter and foods, Faraday discussions 158 (1) (2012) 371–406.

[15] R. Shi, C. Wang, D. Wheeler, X. Liu, Y. Wang, Formation mechanisms of self-organized core/shell and core/shell/corona microstructures in liquid droplets of immiscible alloys, Acta Materialia 61 (4) (2013) 1229–1243.

[16] I.-K. Park, M.-K. Kwon, S.-H. Baek, Y.-W. Ok, T.-Y. Seong, S.-J. Park, Y.-S. Kim, Y.-T. Moon, D.-J. Kim, Enhancement of phase separation in the InGaN layer for self-assembled In-rich quantum dots, Applied Physics Letters 87 (6) (2005) 061906.

[17] A. Nakajima, K. Abe, K. Hashimoto, T. Watanabe, Preparation of hard super-hydrophobic films with visible light transmission, Thin Solid Films 376 (1) (2000) 140–143.

[18] I. M. Lifshitz, V. V. Slyozov, The kinetics of precipitation from supersaturated solid solutions, Journal of Physics and Chemistry of Solids 19 (1) (1961) 35–50.

[19] J. W. Cahn, Phase separation by spinodal decomposition in isotropic systems, The Journal of Chemical Physics 42 (1) (1965) 93–99.

[20] B. R. Wheaton, A. G. Clare, Evaluation of phase separation in glasses with the use of atomic force microscopy, Journal of Non-Crystalline Solids 353 (52) (2007) 4767–4778.

[21] D. Dalmas, A. Lelarge, D. Vandembroucq, Quantitative AFM analysis of phase separated borosilicate glass surfaces, Journal of Non-Crystalline Solids 353 (52-54) (2007) 4672–4680.

[22] L. Martel, M. Allix, F. Millot, V. Sarou-Kanian, E. Véron, S. Ory, D. Massiot, M. Deschamps, Controlling the size of nanodomains in calcium aluminosilicate glasses, The Journal of Physical Chemistry C 115 (39) (2011) 18935–18945.

[23] J. Han, N. Mattern, U. Vainio, A. Shariq, S. Sohn, D. Kim, J. Eckert, Phase separation in Zr56 - x Gd x Co 28 Al 16 metallic glasses $(0 < x < 20)$, Acta Materialia 66 (2014) 262–272.

[24] E. D. Siggia, Late stages of spinodal decomposition in binary mixtures, Physical Review A 20 (2) (1979) 595.

[25] V. Kendon, Inertial effects in three-dimensional spinodal decomposition of a symmetric binary fluid mixture: a lattice Boltzmann study, Journal of Fluid Mechanics 440 (2001) 147–203.

[26] S. Ahmad, S. Das, S. Puri, Kinetics of phase separation in fluids: A molecular dynamics study, Physical Review E 82 (4) (2010) 040107.

[27] D. G. A. L. Aarts, R. P. A. Dullens, H. N. W. Lekkerkerker, Interfacial dynamics in demixing systems with ultralow interfacial tension, New Journal of Physics 7 (40).

[28] A. E. Bailey, W. C. K. Poon, R. J. Christianson, A. B. Schofield, U. Gasser, V. Prasad, S. Manley, P. N. Segre, L. Cipelletti, W. V. Meyer, M. P. Doherty, S. Sankaran, A. L. Jankovsky, W. L. Shiley, J. P. Bowen, J. C. Eggers, C. Kurta, T. Lorik, P. N. Pusey, D. A. Weitz, Spinodal Decomposition in a Model Colloid-Polymer Mixture in Microgravity, Physical Review Letters 99 (20) (2007) 1–4.

[29] L. Sung, A. Karim, J. Douglas, C. Han, Dimensional crossover in the phase separation kinetics of thin poly-

mer blend films, Physical review letters 76 (23) (1996) 4368.

[30] Z. Yuan, B. D. Favis, Coarsening of immiscible co-continuous blends during quiescent annealing, AIChE journal 51 (1) (2005) 271–280.

[31] G. Boiko, N. Bokov, et al., Small-angle scattering and scattering of visible light by sodium-silicate glasses at phase separation, Journal of Non-Crystalline Solids 5 (1) (1970) 41–54.

[32] T. Elmer, M. Nordberg, G. Carrier, E. Korda, Phase separation in borosilicate glasses as seen by electron microscopy and scanning electron microscopy, Journal of The American Ceramic Society 53 (4) (1970) 171–175.

[33] A. Momose, A. Fujii, H. Kadowaki, H. Jinnai, Three-dimensional observation of polymer blend by x-ray phase tomography, Macromolecules 38 (16) (2005) 7197–7200.

[34] M. Roussel, E. Talbot, C. Pareige, R. Pratibha Nalini, F. Gourbilleau, P. Pareige, Confined phase separation in siox nanometric thin layers, Applied Physics Letters 103 (20) (2013) 203109.

[35] J. Baruchel, J.-Y. Buffiere, P. Cloetens, M. Di Michiel, E. Ferrie, W. Ludwig, E. Maire, L. Salvo, Advances in synchrotron radiation microtomography, Scripta Materialia 55 (1) (2006) 41–46.

[36] N. Limodin, L. Salvo, M. Suéry, M. DiMichiel, In situ investigation by X-ray tomography of the overall and local microstructural changes occurring during partial remelting of an Al15.8wt.% Cu alloy, Acta Materialia 55 (9) (2007) 3177–3191.

[37] E. Gouillart, M. J. Toplis, J. Grynberg, M.-H. Chopinet, E. Sondergard, L. Salvo, M. Suéry, M. Di Michiel, G. Varoquaux, In Situ Synchrotron Microtomography Reveals Multiple Reaction Pathways During Soda-Lime Glass Synthesis, Journal of the American Ceramic Society 95 (5) (2012) 1504–1507.

[38] D. Bouttes, E. Gouillart, E. Boller, D. Dalmas, D. Vandembroucq, Fragmentation and Limits to Dynamical Scaling in Viscous Coarsening: An Interrupted in situ X-Ray Tomographic Study, Physical Review Letters 112 (24) (2014) 245701.

[39] E. M. Levin, G. W. Cleek, Shape of Liquid Immiscibility Volume in the System Barium Oxide-Boric Oxide-Silica, Journal of the American Ceramic Society 41 (5) (1958) 175–179.

[40] W.-F. Du, K. Kuraoka, T. Akai, T. Yazawa, Study of Al2O3 effect on structural change and phase separation in Na2O-B2O3-SiO2 glass by NMR, Journal of materials science 35 (19) (2000) 4865–4871.

[41] R. Charles, Dissolution behavior of microporous glass, Journal of the American Ceramic Society 47 (3) (1964) 154–155.

[42] O. Mazurin, M. Streltsina, Determination of tie-line directions in the metastable phase-separation regions of ternary systems, Journal of Non-Crystalline Solids 11 (3) (1972) 199–218.

[43] S. Scholes, F. Wilkinson, Glassy phase separation in sodium borosilicate glasses, Discussions of the Faraday Society 50 (1970) 175–181.

[44] H. Brenner, The slow motion of a sphere through a viscous fluid towards a plane surface, Chemical Engineering Science 16 (1961) 242–251.

[45] A. Dittmar, H. Bornhöft, J. Deubener, Coarsening kinetics in demixed lead borate melts, The Journal of chemical physics 138 (22) (2013) 224502.

[46] L. Wondraczek, J. Deubener, H. del Pozo, A. Habeck, Interfacial Energy in Phase-Separated Glasses from Emulsion Rheology, Journal of the American Ceramic Society 88 (6) (2005) 1673–1675.

[47] A. Mirone, E. Brun, E. Gouillart, P. Tafforeau, J. Kieffer, The pyhst2 hybrid distributed code for high speed tomographic reconstruction with iterative reconstruction and a priori knowledge capabilities, Nuclear Instruments and Methods in Physics Research Section B: Beam Interactions with Materials and Atoms 324 (2014) 41–48.

[48] S. van der Walt, J. L. Schönberger, J. Nunez-Iglesias, F. Boulogne, J. D. Warner, N. Yager, E. Gouillart, T. Yu, scikit-image: image processing in Python., PeerJ 2 (2014) e453.

[49] A. Chambolle, An Algorithm for Total Variation Minimization and Applications, Journal of Mathematical Imaging and Vision 20 (2004) 89–97.

[50] L. Grady, Random walks for image segmentation., IEEE transactions on pattern analysis and machine intelligence 28 (11) (2006) 1768–83.

[51] P. Ramachandran, G. Varoquaux, Mayavi: 3D Visualization of Scientific Data, Computing in Science & Engineering 13 (2) (2011) 40–51.

[52] C. Lang, J. Ohser, R. Hilfer, On the analysis of spatial binary images., Journal of microscopy 203 (2001) 303–313.

[53] S. Torquato, B. Lu, Chord-length distribution function for two-phase random media, Physical Review E 47 (4) (1993) 2950.

[54] P. Levitz, Toolbox for 3D imaging and modeling of porous media: Relationship with transport properties, Cement and Concrete Research 37 (3) (2007) 351–359.

[55] D. Bouttes, Micro-tomographie dun borosilicate de baryum démixé: du mûrissement à la fragmentation, Ph.D. thesis, Paris 6 (2014).

[56] J. Eggers, Nonlinear dynamics and breakup of free-surface flows, Reviews of modern physics 69 (1833) (1997) 865–929.

[57] A. J. Bray, Coarsening dynamics of phase-separating systems., Philosophical transactions. Series A, Mathematical, physical, and engineering sciences 361 (1805) (2003) 781–91; discussion 791–2.

[58] R. Mendoza, J. Alkemper, P. Voorhees, The morphological evolution of dendritic microstructures during coarsening, Metallurgical and Materials Transactions A 34 (3) (2003) 481–489.

[59] D. Kammer, P. Voorhees, The morphological evolution of dendritic microstructures during coarsening, Acta materialia 54 (6) (2006) 1549–1558.

[60] Y. Nishikawa, T. Koga, T. Hashimoto, H. Jinnai, Measurements of Interfacial Curvatures of Bicontinuous Structure from Three-Dimensional Digital Images. 2. A Sectioning and Fitting Method, Langmuir 17 (11) (2001) 3254–3265.

[61] C. R. Lopez-Barron, C. W. Macosko, Characterizing interface shape evolution in immiscible polymer blends via 3D image analysis., Langmuir 25 (16) (2009) 9392–404.

[62] D. Bouttes, E. Gouillart, D. Vandembroucq, Fragmentation-arrested viscous coarsening, *in preparation.*

[63] J. H. Simmons, S. A. Mills, A. Napolitano, Viscous flow in glass during phase separation, Journal of the American Ceramic Society 57 (3) (1974) 109–117.

[64] H. Tanaka, New coarsening mechanisms for spinodal decomposition having droplet pattern in binary fluid mixture: Collision-induced collisions, Physical Review Letters 72 (11) (1994) 1702–1705.

[65] J. C. Russ, R. T. Dehoff, Practical Stereology, Springer US, Boston, MA, 2000.

[66] S. Ahmad, S. Das, S. Puri, Crossover in growth laws for phase-separating binary fluids: Molecular dynamics simulations, Physical Review E 85 (3) (2012) 1–9.

[67] H. Eyring, Viscosity, plasticity, and diffusion as examples of absolute reaction rates, The Journal of chemical physics 4 (4) (1936) 283–291.

[68] J. E. Mungall, Empirical models relating viscosity and tracer diffusion in magmatic silicate melts, Geochimica et Cosmochimica Acta 66 (1) (2002) 125–143.

[69] Y. Liang, F. M. Richter, A. M. Davis, E. B. Watson, Diffusion in silicate melts: I. Self diffusion in CaO-Al2O3-SiO2 at 1500° C and 1 GPa, Geochimica et Cosmochimica Acta 60 (22) (1996) 4353–4367.

[70] V. Zöllmer, K. Rätzke, F. Faupel, A. Meyer, Diffusion in a metallic melt at the critical temperature of mode coupling theory, Physical review letters 90 (19) (2003) 195502.

[71] N. Mattern, G. Goerigk, U. Vainio, M. Miller, T. Gemming, J. Eckert, Spinodal decomposition of Ni-Nb-Y metallic glasses, Acta Materialia 57 (3) (2009) 903–908.

[72] S. Popinet, Gerris: a tree-based adaptive solver for the incompressible Euler equations in complex geometries, Journal of Computational Physics 190 (2) (2003) 572–600.

[73] S. Popinet, An accurate adaptive solver for surface-tension-driven interfacial flows, Journal of Computational Physics 228 (2009) 5838–5866.